


Activity-induced droplet propulsion and multifractality

Nadia Bihari Padhan^{*} and Rahul Pandit[†]

Centre for Condensed Matter Theory, Department of Physics, Indian Institute of Science, Bangalore 560012, India

 (Received 11 September 2022; accepted 19 June 2023; published 21 July 2023)

We elucidate the crucial role that confinement plays in collective and emergent behaviors in active- or living-matter systems by developing a minimal hydrodynamic model, without an orientational order parameter, for assemblies of contractile swimmers encapsulated in a droplet of a binary-fluid emulsion. Our model uses two coupled scalar order parameters, ϕ and ψ , which capture, respectively, the droplet interface and the activity of the contractile swimmers inside this droplet. These order parameters are also coupled to the velocity field \mathbf{u} . At low activity, our model yields a self-propelling droplet whose center of mass (CM) displays rectilinear motion, powered by the spatiotemporal evolution of the field ψ , which leads to a time-dependent vortex dipole at one end of the droplet. As we increase the activity, this CM shows chaotic superdiffusive motion, which we characterize by its mean-square displacement; and the droplet interface exhibits multifractal fluctuations, whose spectrum of exponents we calculate. We explore the implications of our results for experiments on active droplets of contractile swimmers.

DOI: [10.1103/PhysRevResearch.5.L032013](https://doi.org/10.1103/PhysRevResearch.5.L032013)

Active matter comprises systems that are far from equilibrium and in which the constituents extract energy from their surroundings, do mechanical work, and dissipate energy to the same environment [1–4]. The self-organization of the constituents of such systems can lead to large-scale pattern formation, observed in, e.g., crowds [5,6], fish schools [7], bird flocks [8,9], and bacterial colonies [10]. They exhibit a variety of fascinating emergent phenomena, e.g., motility-induced phase separation (MIPS), in which an initially uniform state of active swimmers separates spontaneously into dense and dilute phases, driven by persistent motion and repulsion [11–13]. These studies of MIPS have been limited to unbounded domains; but most experiments, with motile bacteria or synthetic microswimmers, use confinement—solid immovable or soft, e.g., by a droplet boundary—that plays a key role in the formation of spatiotemporal patterns in assemblies of active microswimmers [14–16].

We develop a phase-field model to study MIPS in assemblies of contractile swimmers encapsulated in a binary-fluid emulsion droplet. At low activity, we obtain a self-propelling droplet whose center of mass (CM) displays rectilinear motion, powered by the spatiotemporal evolution of an active scalar field, which leads to a time-dependent vortex dipole at one end of the droplet. With increasing activity, this CM

displays superdiffusive motion that is driven by active turbulence. Such motion is reminiscent of a Lévy walk [17], which has been obtained in recent experiments on chemically active droplets [18]. The droplet interface exhibits multifractal fluctuations. This propulsion does not require any orientational ordering, unlike that in studies with active droplets powered by active nematics or polar gels [19–21]. Our results are of direct relevance to droplets of contractile swimmers such as *Chlamydomonas reinhardtii* [22,23] (*C. reinhardtii*) and synthetic active colloids [24,25].

The phase-field theory that we develop has two conserved scalar order parameters, ϕ and ψ . The former distinguishes between two coexisting liquid phases, separated by an interface at the droplet boundary; the latter is related to the microswimmers concentration. ϕ and ψ are coupled to each other and to the flow velocity \mathbf{u} , as in the Cahn-Hilliard-Navier-Stokes (CHNS) system or model H [26,27]. In the absence of the direct coupling between the two order parameters, our model decouples into (a) the CHNS model, for ϕ and \mathbf{u} , that has been used to study multifractal droplet dynamics [26] in a turbulent flow and (b) the *active model H*, for ψ and \mathbf{u} , that has been used to study MIPS [11,28,29].

We carry out pseudospectral direct numerical simulations (DNSs) of our model to uncover the dependence of the spatiotemporal evolution of an emergent active droplet on the *activity* parameter A (defined below). For low values of A , the center of mass (CM) of the droplet shows rectilinear motion, associated with a time-dependent vortex dipole at one of its ends; as A increases, the droplet fluctuates and its CM exhibits a crossover from rectilinear to superdiffusive motion, reminiscent of Lévy walks [18,30–33]. Furthermore, at large values of A , the bacterial field generates low Reynolds number, but turbulent flows and *multifractal deformation* of the active-droplet boundary.

^{*}nadia@iisc.ac.in[†]rahul@iisc.ac.in

We use

$$\mathcal{F}[\phi, \nabla\phi, \psi, \nabla\psi] = \int_{\Omega} \left\{ \frac{3}{16} \left[\frac{\sigma_1}{\epsilon_1} (\phi^2 - 1)^2 + \frac{\sigma_2}{\epsilon_2} (\psi^2 - 1)^2 \right] - \beta\phi\psi + \frac{3}{4} (\sigma_1\epsilon_1 |\nabla\phi|^2 + \sigma_2\epsilon_2 |\nabla\psi|^2) \right\} d\Omega, \quad (1)$$

where Ω is the region we consider and \mathcal{F} is a Landau-Ginzburg-type free-energy functional, whose first term is a double-well potential, for the ϕ field, with minima at $\phi = \pm 1$ corresponding to two pure binary-fluid phases, which are separated by a smooth interface of width ϵ_1 and surface tension σ_1 [as in the statistical mechanics of binary mixtures (see, e.g., Ref. [34])]. For *binary-fluid mixtures*, the CHNS equations were derived from phenomenological arguments (see, e.g., Ref. [35], which referred to CHNS as model H). In the generalized-CHNS model that we employ, the second term in \mathcal{F} is a double-well potential for the ψ field, with minima at $\psi = \pm 1$ corresponding to dense and dilute phases of the microswimmers, which are separated by a smooth interface of width ϵ_2 and surface tension σ_2 (as, e.g., in the study of MIPS in Ref. [28]). The attractive coupling $\beta > 0$ favors configurations in which ϕ and ψ have the same sign. To address experiments on active droplets carried out under planar confinement, we use the following two-dimensional (2D) *active* CHNS equations [see the Supplemental Material (SM) [36] for our CHNS formalism]:

$$\partial_t \phi + (\mathbf{u} \cdot \nabla)\phi = M_1 \nabla^2 \left(\frac{\delta \mathcal{F}}{\delta \phi} \right), \quad (2)$$

$$\partial_t \psi + (\mathbf{u} \cdot \nabla)\psi = M_2 \nabla^2 \left(\frac{\delta \mathcal{F}}{\delta \psi} \right), \quad (3)$$

$$\partial_t \omega + (\mathbf{u} \cdot \nabla)\omega = \nu \nabla^2 \omega - \alpha \omega + [\nabla \times (\mathfrak{S}^\phi + \mathfrak{S}^\psi)], \quad (4)$$

$$\nabla \cdot \mathbf{u} = 0; \quad \omega = (\nabla \times \mathbf{u}), \quad (5)$$

$$\mathfrak{S}^\phi = -(3/2)\sigma_1\epsilon_1 \nabla^2 \phi \nabla \phi, \quad (6)$$

$$\mathfrak{S}^\psi = -(3/2)\tilde{\sigma}_2\epsilon_2 \nabla^2 \psi \nabla \psi, \quad (7)$$

where the constant fluid density $\rho = 1$, the advection-diffusion equations (2) and (3) use the constant mobilities M_1 and M_2 for ϕ and ψ , respectively, and the 2D incompressible Navier-Stokes equations (4) and (5) use the vorticity ω , the kinematic viscosity ν , and the bottom friction α . In addition, the interfacial stress \mathfrak{S}^ϕ [Eq. (6)] from ϕ is derived from \mathcal{F} ; for the *active stress* \mathfrak{S}^ψ [Eq. (7)] from ψ , we use the active-model-H formulation for MIPS [11,28,29]; both ω and $[\nabla \times (\mathfrak{S}^\phi + \mathfrak{S}^\psi)]$ lie normal to the 2D plane. We refer to ψ as the active scalar [37]. Note that the mechanical surface tension $\tilde{\sigma}_2 \neq \sigma_2$; and $\tilde{\sigma}_2$ can take both negative and positive values, unlike σ_1 and σ_2 which are always positive. For contractile (extensile) swimmers, $\tilde{\sigma}_2 < 0$ ($\tilde{\sigma}_2 > 0$) and the system shows arrested phase separation (complete phase separation) [28]. The spatiotemporal evolution of the fields in Eqs. (1)–(7) depends on the initial conditions (see below) and the nondimensional Cahn numbers $Cn_1 = \epsilon_1/R_0$ and $Cn_2 = \epsilon_2/R_0$, Weber numbers $We_1 = R_0 U_0^2/\sigma_1$ and $We_2 = R_0 U_0^2/\sigma_2$, Peclet numbers $Pe_1 = R_0 U_0 \epsilon_1/(M_1 \sigma_1)$ and

$Pe_2 = R_0 U_0 \epsilon_2/(M_2 \sigma_2)$, order-parameter couplings $\beta'_1 = \beta \epsilon_1/\sigma_1$ and $\beta'_2 = \beta \epsilon_2/\sigma_2$, friction $\alpha' = \alpha R_0/U_0$, Reynolds number $Re = R_0 U_0/\nu$, where $U_0 = \langle U_{CM}(t) \rangle_t$, with U_{CM} the speed of the droplet's center of mass (CM) (see below and the Supplemental Material (SM) [36]), and, most importantly, the *activity*

$$A = |\tilde{\sigma}_2|/\sigma_2. \quad (8)$$

We concentrate on contractile swimmers with $\tilde{\sigma}_2 < 0$. In Table I of the SM [36], we list the parameters for our DNS runs R1–R7.

We consider an initially stationary and circular droplet, of radius R_0 , and with its center at $(x_{0,1}, x_{0,2}) = (\pi, \pi)$,

$$\mathbf{u}(\mathbf{x}, t = 0) = 0,$$

$$\phi(\mathbf{x}, t = 0) = \tanh \left(\frac{R_0 - \sqrt{(x_1 - x_{0,1})^2 + (x_2 - x_{0,2})^2}}{\epsilon_1} \right),$$

$$\psi(\mathbf{x}, t = 0) = \begin{cases} \psi_0(\mathbf{x}) & \text{for } |\mathbf{x}| \leq R_0 \\ -1 & \text{for } |\mathbf{x}| > R_0, \end{cases} \quad (9)$$

and $\psi_0(\mathbf{x})$ is a random number distributed uniformly on the interval $[-0.1, 0.1]$. Regions with negative (positive) values of ϕ and ψ have low (high) densities of these scalars.

Our DNS of Eqs. (1)–(7) employs a standard Fourier pseudospectral method [38], with the 1/2 rule for the removal of aliasing errors. We use a square domain of side $L = 2\pi$, with periodic boundary conditions in both spatial directions, and N^2 collocation points. For time integration, we use the semi-implicit exponential time differencing Runge-Kutta-2 (ETDRK-2) method [39]. Our computer program is written in CUDA C and is optimized for recent GPU architectures, such as the one used in the NVIDIA A100 processor.

To monitor the spatiotemporal evolution of the initial droplet [Eq. (9)], we obtain pseudocolor plots of ϕ and ψ (Fig. 1) and we compute

$$U_{CM}(t) = \sqrt{\sum_{i=1}^2 \left[\sum_{\mathbf{x} \ni \phi(\mathbf{x}, t) > 0} u_i(\mathbf{x}, t) \right]^2},$$

$$E(k, t) = \frac{1}{2} \sum_{k-1/2 < k' < k+1/2} [\hat{\mathbf{u}}(\mathbf{k}', t) \cdot \hat{\mathbf{u}}(-\mathbf{k}', t)],$$

$$S_\psi(k, t) = \sum_{k-1/2 < k' < k+1/2} |\hat{\psi}(\mathbf{k}', t)|^2,$$

$$S_\phi(k, t) = \sum_{k-1/2 < k' < k+1/2} |\hat{\phi}(\mathbf{k}', t)|^2,$$

$$\mathcal{L}(t) = 2\pi \sum_k S_\psi(k, t) / \sum_k k S_\psi(k, t),$$

$$\mathcal{M}(t) = \left\langle \sum_{i=1}^2 [x_{CM,i}(t) - x_{CM,i}(t_0)]^2 \right\rangle,$$

$$\Gamma(t) = [S(t)/S_0(t)] - 1, \quad (10)$$

which are, respectively, the speed of the droplet's CM, the fluid energy spectrum, the spectra of ψ and ϕ , a length scale that follows from S_ψ , the mean-square displacement of the droplet's CM, and the normalized perimeter of the $\phi = 0$

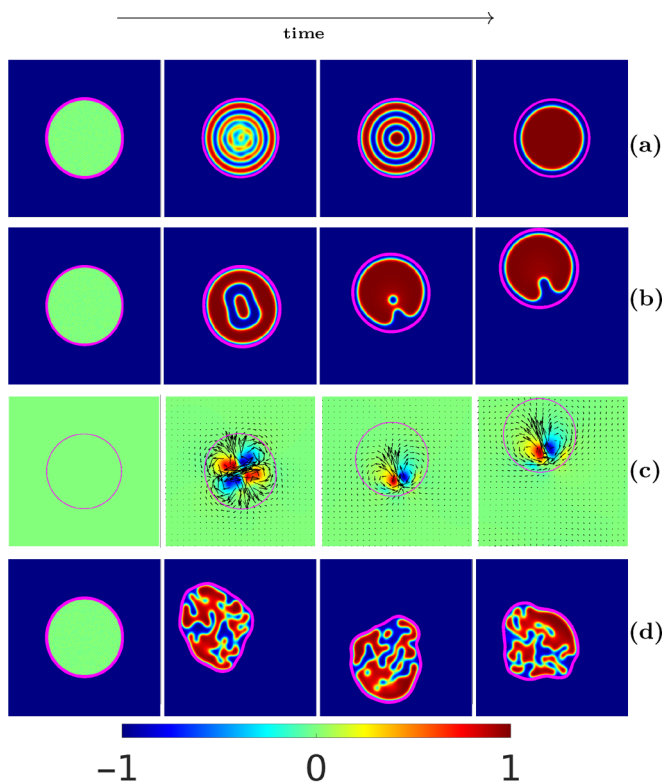


FIG. 1. Illustrative pseudocolor plots of ψ , with the $\phi = 0$ contour shown in magenta, at different representative times (increasing from left to right) for (a) $A = 0$ (no droplet propulsion), (b) $A = 0.15$ (rectilinear droplet propulsion), and (d) $A = 1$ (turbulent droplet propulsion). In (c), we show, for $A = 0.15$, vector plots of the velocity field \mathbf{u} , with the $\phi = 0$ contour line (magenta), overlaid on a pseudocolor plot of the vorticity ω normalized by its maximal value; the lengths of the velocity vectors are proportional to their magnitudes. (See videos V1–V4 in the SM [36].)

contour that bounds the droplet [$S(t)$ is the perimeter of the droplet at time t and $S_0(t)$ is the perimeter of a circular droplet of equal area at time t]. The subscripts i and CM denote Cartesian components and the droplet's CM, respectively, carets indicate spatial Fourier transform, and k and k' are the moduli of the wave vectors \mathbf{k} and \mathbf{k}' .

In Fig. 1, we illustrate the evolution of the initial droplet [Eq. (9)] via pseudocolor plots of ψ and the $\phi = 0$ contour (in magenta), at different representative times and $A = 0$ [row (a)], $A = 0.15$ [row (b)], and $A = 1$ [row (d)]; in row (c), we show, for $A = 0.15$, vector plots of the velocity field \mathbf{u} , with the $\phi = 0$ contour line, overlaid on a pseudocolor plot of the vorticity ω normalized by its maximal value. Case $A = 0$ [row (a)]: there is no mean flow, i.e., $U_{CM}(t) = 0$ for all t ; however, as time increase (from left to right), the initially homogeneous mixture of active matter becomes unstable and undergoes phase separation via the formation of self-organized alternating rings of regions with positive and negative values of ψ (cf. oil-water phase separation in a microfluidic droplet [40]). Eventually, complete phase separation occurs, via successive ring collapses, and we obtain a $\psi > 0$ region (red) surrounded by a $\psi < 0$ ring (blue) inside the $\phi = 0$ contour.

As we increase A , we find a remarkable transition to a *self-propelling droplet*, whose motion we depict, for the il-

lustrative value $A = 0.15$, via pseudocolor plots in Figs. 1(b) and the video V2 in the SM [36]. Initially, phase separation tries to set in, but is partially arrested. At this stage the flow field is dominated by a vortex quadrupole [second panels in Figs. 1(b) and 1(c)]. Thereafter, an umbilicus, which forms at one end of the droplet, oscillates periodically in time as it shoots out a tiny blue bead, with $\psi < 0$ [third and fourth panels in Fig. 1(b)]. The associated flow patterns contain an oscillating vortex dipole (third and fourth panels in Fig. 1(c) and the video V3 in the SM [36]) that propels the droplet along a straight line [the orange trajectory in Fig. 2(b)] [41]. These oscillations are mirrored in the periodic time dependence of $\mathcal{L}(t)/R_0$ [magenta curve in Fig. 2(a)] and $U_{CM}(t)$ [magenta curve in Fig. 3(a)], and also in a limit cycle whose projection can be viewed in the $\mathcal{L}(t) - U_{CM}(t)$ plane (magenta curve in Fig. 1(a) in the SM [36]). Thus, as we increase A , the initial transition from a static to a self-propelling droplet can be associated with the formation of a stable limit cycle. Self-propulsion is a consequence of the arrested phase separation, which leads to a nonisotropic distribution of the active field ψ .

For sufficiently large A ($\gtrsim 0.5$), statistically steady *active-fluid turbulence* develops inside the droplet and leads to important modifications in its structure and propulsion: (a) We find a significant suppression of the phase separation of the active scalar [Figs. 1(d)], which is reminiscent of turbulence-induced coarsening arrest in a binary-fluid mixture [27]; (b) chaotic temporal fluctuations in $\mathcal{L}(t)/R_0$ [Fig. 2(a)]; (c) convoluted trajectories of the CM of the droplet [e.g., the blue-purple trajectory in Fig. 2(b)], which are accompanied by chaotic temporal fluctuations in $U_{CM}(t)$ [Fig. 3(a)], and the projections of the phase-space trajectories in the $\mathcal{L}(t) - U_{CM}(t)$ plane (red and green curves in Fig. 1(a) in the SM [36]); (d) multifractal fluctuations of $\Gamma(t)$ [Figs. 3(d)–3(f)]; (e) the energy, ϕ , and ψ spectra that extend over a large range of the wave number k (Figs. 2(a)–2(c) in the SM [36]).

The transition from rectilinear to chaotic-droplet trajectories is apparent in the illustrative plots of droplet-CM paths, for $A = 0.15$ (orange) and $A = 1$ (blue-purple), in Fig. 2(b), which we compute as in Ref. [42] (see the SM [36]). From such paths, we obtain the normalized mean-square displacement $\mathcal{M}(t)/R_0^2$, which we present in log-log plots versus the nondimensional time t in Fig. 2(c): rectilinear droplet motion leads to $\mathcal{M}(t) \sim t^2$ (red curve for $A = 0.15$). As we increase A , we obtain crossovers to superdiffusive behaviors, which are consistent with $\mathcal{M}(t) \sim t^{5/3}$ (green curve for $A = 0.5$) and $\mathcal{M}(t) \sim t^{4/3}$ (magenta curve for $A = 2$), which suggest Lévy walks for the droplet's CM (cf. the experimental results on chemically active droplets [18] and swarming bacteria [30]). The activity-induced transition from rectilinear to chaotic droplet motion is also mirrored in the time dependence of $U_{CM}(t)/U_0$ that we depict in Fig. 3(a): the oscillatory behavior at $A = 0.15$ (magenta curve) gives way to a chaotic times series as we move from $A = 0.5$ (green) to $A = 1$ (blue). We characterize these chaotic fluctuations by computing the probability distribution function (PDF) $\mathcal{P}(U_{CM}/U_0)$, which we show in the semilogarithmic plots of Fig. 3(b). These PDFs collapse onto each other, for different values of A , because we use the scaled speed U_{CM}/U_0 ; if we use the unscaled U_{CM} ,

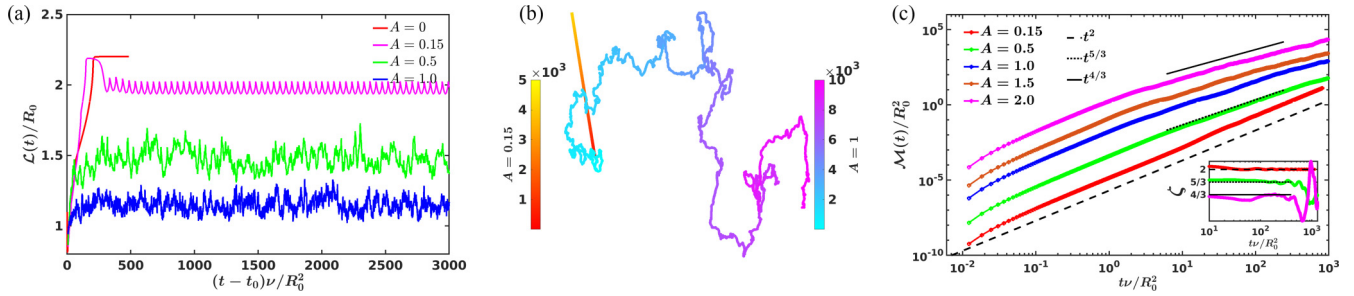


FIG. 2. (a) Plots of $\mathcal{L}(t)/R_0$ [Eq. (10)] vs $(t - t_0)v/R_0^2$ for $A = 0$ (red curve), $A = 0.15$ (magenta curve), $A = 0.5$ (green curve), and $A = 1$ (blue curve), with t_0 is a nonuniversal offset that depends on A . (b) Illustrative trajectories of the droplet's CM for $A = 0.15$ (orange) and $A = 1$ (blue-purple), with color bars indicating the simulation time. (c) Log-log plots of the mean-square displacement $\mathcal{M}(t)$ vs tv/R_0^2 (after the removal of initial transients) for droplet-CM trajectories: $A = 0.15$ (red), $A = 0.5$ (green), $A = 1$ (blue), $A = 1.5$ (dark orange), and $A = 2$ (magenta). Initially these plots show ballistic regimes, but, at large times, we see $\mathcal{M}(t) \sim t^\zeta$, with $\zeta = 2$ (rectilinear motion for $A = 0.15$), and superdiffusive regimes with $\zeta = 1.67 \pm 0.02 \simeq 5/3$ (for $A = 0.5$) and $\zeta = 1.28 \pm 0.05 \simeq 4/3$ (for $A = 2$) via local-slope analysis (the inset shows plots of ζ vs t). Plots for different values of A are displaced vertically for ease of visualization.

then the skewness of this PDF increases with A (Fig. 1(c) in the SM [36]). Furthermore, U_0 increases monotonically with A [Fig. 3(c)] and shows signs of saturation at large A .

Not only does the active droplet display an increase in U_0 with A , but it also exhibits, as A increases, an enhancement in fluctuations in its normalized perimeter $\Gamma(t)$ [Eq. (10)], which we plot versus tv/R_0^2 in Fig. 3(d). These fluctuations of Γ lead to broad PDFs, $\mathcal{P}_\Gamma(\Gamma)$, which we present in Fig. 3(e), for $A = 0.5$ (green), $A = 0.75$ (magenta), $A = 1$ (red), and $A = 1.5$ (blue); the widths and skewnesses of these PDFs increase with A (see the SM [36]). From a multifractal analysis of the time series $\Gamma(t)$, we obtain the generalized spectrum of dimensions $D(h)$ as a function of the Hurst exponent h by using the wavelet-leader method (see Refs. [43,44] and the SM [36]). The generalized dimension $D(h)$ is the Legendre transform of the generalized exponent $\tau(q)$, with $h(q) = d\tau(q)/dq$, the

generalized Hurst exponent of order q (see Eqs. (15) and (16) in the Supplemental Material [36]). $D(h)$ characterizes the multifractal properties of the time series, i.e., it measures the fractal dimension of a signal at different scales. In Fig. 3(f), we present an illustrative plot of the multifractal spectrum $D(h)$ for $A = 1.5$ (blue curve), where $0.7 \lesssim h \lesssim 1.5$, so the time series we consider has long-term memory (note that $h = 0.5$ for the Brownian case). Such multifractality has not been obtained heretofore for active droplets; it is akin to the recently discovered droplet-perimeter fluctuations in turbulent binary-fluid flows [26].

As the activity induces turbulence in the ψ field, the droplet's motion yields fluid turbulence, which we characterize by the energy, ϕ , and ψ spectra $E(k, t)$, $S_\phi(k, t)$, and $S_\psi(k, t)$ [Eq. (10)], which we plot in Figs. 2(a)–2(c) of the SM [36] for $A = 0.5, 1$, and 1.5 . Even though the Reynolds num-

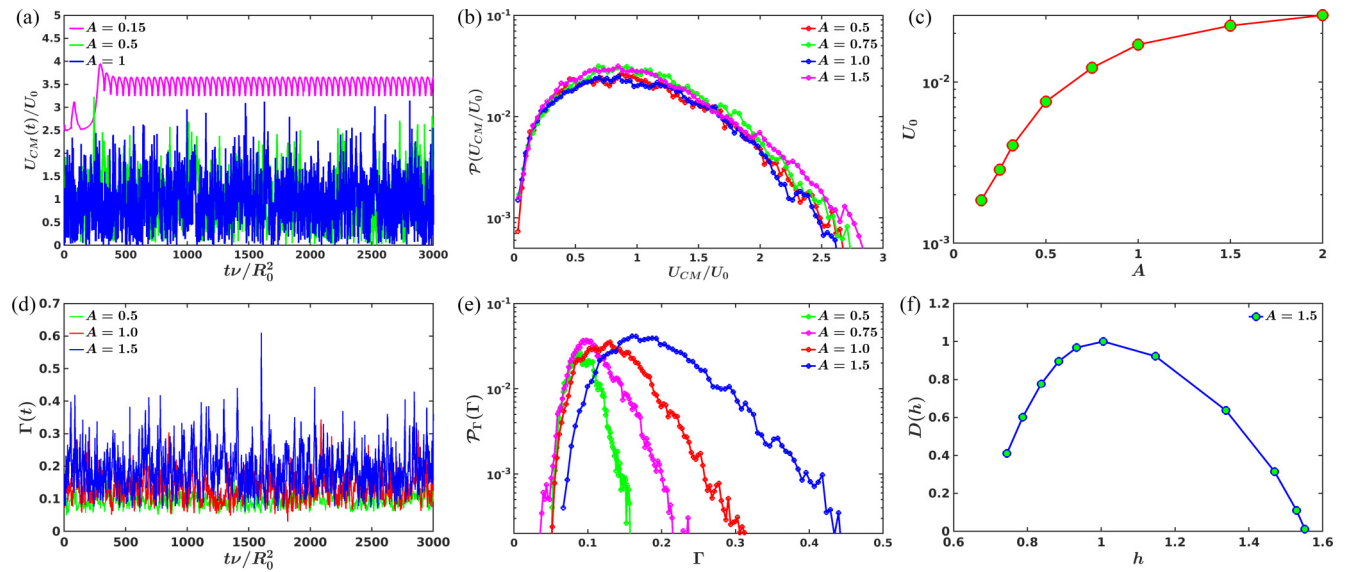


FIG. 3. (a) Plots vs the nondimensionalized time tv/R_0^2 of the scaled droplet-CM speed U_{CM}/U_0 [Eq. (10)] for $A = 0.15$ (magenta curve, which has been moved up to aid visualization), $A = 0.5$ (green), and $A = 1$ (blue). (b) Semilogarithmic plots of the PDF $\mathcal{P}(U_{CM}/U_0)$ for $A = 0.5$ (red), $A = 0.75$ (green), $A = 1$ (blue), and $A = 1.5$ (magenta). (c) Semilogarithmic plot of U_0 vs A . (d) Plots vs tv/R_0^2 of the normalized droplet perimeter $\Gamma(t)$ [Eq. (10)] for $A = 0.5$ (green), $A = 1$ (red), and $A = 1.5$ (blue). (e) Semilogarithmic plots of the PDF of $\mathcal{P}_\Gamma(\Gamma)$ for $A = 0.5$ (green), $A = 0.75$ (magenta), $A = 1$ (red), and $A = 1.5$ (blue). (f) Plots of the multifractal $D(h)$ vs the Hurst exponent h (see text), obtained from $\Gamma(t)$, for $A = 1.5$.

bers are small, these spectra span several decades in k , i.e., a clear signature of turbulence. We will present elsewhere [45] a detailed study of the properties of a statistically homogeneous and isotropic form of this turbulence, which is reminiscent of bacterial or active-fluid turbulence [33,46,47] and elastic turbulence in polymer solutions [48,49].

We have developed a minimal model for assemblies of contractile swimmers, without alignment interactions, encapsulated in a droplet of a binary-fluid emulsion. Our hydrodynamic model, with the scalar order parameter ϕ and the active scalar ψ coupled to each other and the velocity field \mathbf{u} , not only captures the droplet interface (via the $\phi = 0$ contour) and its fluctuations, but also leads to droplet self-propulsion, which is rectilinear at low A ($\simeq 0.15$) and chaotic for large values of A , at which the CM of the droplet shows superdiffusive motion and the droplet interface exhibits multifractal fluctuations. Our study is distinct from earlier experimental and theoretical studies of active droplets that consider cell-level models in nematically ordered, active polar, chemically driven, or phase-field systems [19–21,50–62]. Specifically, the phase-field model of Ref. [54] utilizes two scalar fields to model the behavior of the cytoplasm and the contractile material within the droplet. In this model, the self-propulsion of a droplet is determined by a stress term in the Stokes equation, which is a function of both scalar

fields. This stress term induces an inhomogeneous surface tension (on the droplet's interface) and leads to Marangoni flows. By contrast, the activity-induced droplet propulsion in our model arises from the interplay of ϕ , \mathbf{u} , and a collection of contractile swimmers, which are described via the field ψ and are enclosed inside the droplet. This propulsion shows a crossover from rectilinear to superdiffusive motion of the droplet CM. The stress terms for the ϕ and ψ fields are independent of each other. The ψ field captures the MIPS in contractile swimmers and, when phase separation is arrested because this field is *confined to a droplet*, self-propulsion arises from the nonisotropic distribution of the active material.

We look forward to the experimental verification of our results, especially in droplets of contractile swimmers such as *C. reinhardtii* [22,23] or active colloids [24,25]. The emergent motility that we uncover for the active droplet in our model indicates that it should be possible to engineer novel self-propelling robotic materials with active constituents that are confined within soft boundaries.

We thank J. K. Alageshan, K. V. Kiran, S. K. Choudhary, S. J. Kole, and S. Ramaswamy for discussions, the National Supercomputing Mission (NSM) Grant No. DST/NSM/R&D_-HPC_Applications/2021/34 and SERB (India) for financial support, and SERC (IISc) for computational resources.

-
- [1] S. Ramaswamy, Active matter, *J. Stat. Mech.* (2017) 054002.
- [2] M. J. Bowick, N. Fakhri, M. C. Marchetti, and S. Ramaswamy, Symmetry, Thermodynamics, and Topology in Active Matter, *Phys. Rev. X* **12**, 010501 (2022).
- [3] M. C. Marchetti, J.-F. Joanny, S. Ramaswamy, T. B. Liverpool, J. Prost, M. Rao, and R. A. Simha, Hydrodynamics of soft active matter, *Rev. Mod. Phys.* **85**, 1143 (2013).
- [4] B. Mahault, Outstanding problems in the statistical physics of active matter, Ph.D. thesis, Universite Paris-Saclay, 2018.
- [5] C. Castellano, S. Fortunato, and V. Loreto, Statistical physics of social dynamics, *Rev. Mod. Phys.* **81**, 591 (2009).
- [6] A. Bottinelli, D. T. J. Sumpter, and J. L. Silverberg, Emergent Structural Mechanisms for High-Density Collective Motion Inspired by Human Crowds, *Phys. Rev. Lett.* **117**, 228301 (2016).
- [7] C. Becco, N. Vandewalle, J. Delcourt, and P. Poncin, Experimental evidences of a structural and dynamical transition in fish school, *Physica A* **367**, 487 (2006).
- [8] W. Bialek, A. Cavagna, I. Giardina, T. Mora, E. Silvestri, M. Viale, and A. M. Walczak, Statistical mechanics for natural flocks of birds, *Proc. Natl. Acad. Sci.* **109**, 4786 (2012).
- [9] A. Cavagna, A. Cimarelli, I. Giardina, G. Parisi, R. Santagati, F. Stefanini, and M. Viale, Scale-free correlations in starling flocks, *Proc. Natl. Acad. Sci.* **107**, 11865 (2010).
- [10] C. Chen, S. Liu, X.-q. Shi, H. Chate, and Y. Wu, Weak synchronization and large-scale collective oscillation in dense bacterial suspensions, *Nature (London)* **542**, 210 (2017).
- [11] R. Wittkowski, A. Tiribocchi, J. Stenhammar, R. J. Allen, D. Marenduzzo, and M. E. Cates, Scalar field theory for active-particle phase separation, *Nat. Commun.* **5**, 4351 (2014).
- [12] M. E. Cates and J. Tailleur, Motility-induced phase separation, *Annu. Rev. Condens. Matter Phys.* **6**, 219 (2015).
- [13] G. Gonnella, D. Marenduzzo, A. Suma, and A. Tiribocchi, Motility-induced phase separation and coarsening in active matter, *C. R. Phys.* **16**, 316 (2015).
- [14] H. Wioland, F. G. Woodhouse, J. Dunkel, J. O. Kessler, and R. E. Goldstein, Confinement Stabilizes a Bacterial Suspension into a Spiral Vortex, *Phys. Rev. Lett.* **110**, 268102 (2013).
- [15] D. Huang, Y. Du, H. Jiang, and Z. Hou, Emergent spiral vortex of confined biased active particles, *Phys. Rev. E* **104**, 034606 (2021).
- [16] G. Ramos, M. L. Cordero, and R. Soto, Bacteria driving droplets, *Soft Matter* **16**, 1359 (2020).
- [17] V. Zaburdaev, S. Denisov, and J. Klafter, Lévy walks, *Rev. Mod. Phys.* **87**, 483 (2015).
- [18] V. S. Akella, R. Rajesh, and M. V. Panchagnula, Lévy walking droplets, *Phys. Rev. Fluids* **5**, 084002 (2020).
- [19] T. Gao and Z. Li, Self-Driven Droplet Powered By Active Nematics, *Phys. Rev. Lett.* **119**, 108002 (2017).
- [20] E. Tjhung, D. Marenduzzo, and M. E. Cates, Spontaneous symmetry breaking in active droplets provides a generic route to motility, *Proc. Natl. Acad. Sci.* **109**, 12381 (2012).
- [21] L. J. Ruske and J. M. Yeomans, Morphology of Active Deformable 3D Droplets, *Phys. Rev. X* **11**, 021001 (2021).
- [22] J. M. Yeomans, D. O. Pushkin, and H. Shum, An introduction to the hydrodynamics of swimming microorganisms, *Eur. Phys. J.: Spec. Top.* **223**, 1771 (2014).
- [23] A. A. Fragkopoulos, J. Vachier, J. Frey, F.-M. Le Menn, M. G. Mazza, M. Wilczek, D. Zwicker, and O. Baumchen, Self-generated oxygen gradients control collective aggregation of photosynthetic microbes, *J. R. Soc., Interface* **18**, 20210553 (2021).
- [24] A. Zöttl and H. Stark, Emergent behavior in active colloids, *J. Phys.: Condens. Matter* **28**, 253001 (2016).

- [25] J. R. Howse, R. A. L. Jones, A. J. Ryan, T. Gough, R. Vafabakhsh, and R. Golestanian, Self-Motile Colloidal Particles: From Directed Propulsion to Random Walk, *Phys. Rev. Lett.* **99**, 048102 (2007).
- [26] N. Pal, P. Perlekar, A. Gupta, and R. Pandit, Binary-fluid turbulence: Signatures of multifractal droplet dynamics and dissipation reduction, *Phys. Rev. E* **93**, 063115 (2016).
- [27] P. Perlekar, N. Pal, and R. Pandit, Two-dimensional turbulence in symmetric binary-fluid mixtures: Coarsening arrest by the inverse cascade, *Sci. Rep.* **7**, 44589 (2017).
- [28] A. Tiribocchi, R. Wittkowski, D. Marenduzzo, and M. E. Cates, Active Model H: Scalar Active Matter in a Momentum-Conserving Fluid, *Phys. Rev. Lett.* **115**, 188302 (2015).
- [29] M. R. Shaebani, A. Wysocki, R. G. Winkler, G. Gompper, and H. Rieger, Computational models for active matter, *Nat. Rev. Phys.* **2**, 181 (2020).
- [30] G. Ariel, A. Rabani, S. Benisty, J. D. Partridge, R. M. Harshey, and A. Be'er, Swarming bacteria migrate by Lévy walk, *Nat. Commun.* **6**, 8396 (2015).
- [31] G. Ariel, A. Be'er, and A. Reynolds, Chaotic Model for Lévy Walks in Swarming Bacteria, *Phys. Rev. Lett.* **118**, 228102 (2017).
- [32] D. Elhmaïdi, A. Provenzale, and A. Babiano, Elementary topology of two-dimensional turbulence from a lagrangian viewpoint and single-particle dispersion, *J. Fluid Mech.* **257**, 533 (1993).
- [33] S. Mukherjee, R. K. Singh, M. James, and S. S. Ray, Anomalous Diffusion and Lévy Walks Distinguish Active from Inertial Turbulence, *Phys. Rev. Lett.* **127**, 118001 (2021).
- [34] P. M. Chaikin, T. C. Lubensky, and T. A. Witten, *Principles of Condensed Matter Physics*, Vol. 10 (Cambridge University Press, Cambridge, 1995).
- [35] P. C. Hohenberg and B. I. Halperin, Theory of dynamic critical phenomena, *Rev. Mod. Phys.* **49**, 435 (1977).
- [36] See Supplemental Material at <http://link.aps.org/supplemental/10.1103/PhysRevResearch.5.L032013> for the detailed calculations, simulation parameters, additional figures, and details of the supplemental movies.
- [37] The active-matter terminology and the conventional fluid-dynamics nomenclature are slightly different. In the fluid-dynamics sense, both ϕ and ψ are active scalars insofar as they affect the velocity field \mathbf{u} . However, in the active-matter sense, ψ is active but ϕ is not.
- [38] C. Canuto, M. Y. Hussaini, A. Quarteroni, A. Thomas Jr. *et al.*, *Spectral Methods in Fluid Dynamics* (Springer Science Business Media, New York, 2012).
- [39] S. M. Cox and P. C. Matthews, Exponential time differencing for stiff systems, *J. Comput. Phys.* **176**, 430 (2002).
- [40] P. G. Moerman, P. C. Hohenberg, E. Vanden-Eijnden, and J. Brujic, Emulsion patterns in the wake of a liquid-liquid phase separation front, *Proc. Natl. Acad. Sci.* **115**, 3599 (2018).
- [41] We have explicitly checked that the precise direction of droplet propulsion depends on the realization of the random distribution of $\psi_0(x)$ in the initial condition.
- [42] L. Bai and D. Breen, Calculating center of mass in an unbounded 2d environment, *J. Graph. Tools* **13**, 53 (2008).
- [43] S. Jaffard, B. Lashermes, and P. Abry, Wavelet leaders in multifractal analysis, in *Wavelet Analysis and Applications* (Springer, New York, 2006), pp. 201–246.
- [44] H. Wendt and P. Abry, Multifractality tests using bootstrapped wavelet leaders, *IEEE Trans. Signal Proc.* **55**, 4811 (2007).
- [45] N. Padhan, K. Kiran, and R. Pandit, Homogeneous and isotropic turbulence in the active Cahn-Hilliard-Navier-Stokes model (unpublished).
- [46] R. Alert, J. Casademunt, and J.-F. Joanny, Active turbulence, *Annu. Rev. Condens. Matter Phys.* **13**, 143 (2022).
- [47] K. V. Kiran, A. Gupta, A. K. Verma, and R. Pandit, Irreversibility in bacterial turbulence: Insights from the mean-bacterial-velocity model, *Phys. Rev. Fluids* **8**, 023102 (2023).
- [48] A. Groisman and V. Steinberg, Elastic turbulence in a polymer solution flow, *Nature (London)* **405**, 53 (2000).
- [49] A. Gupta and R. Pandit, Melting of a nonequilibrium vortex crystal in a fluid film with polymers: Elastic versus fluid turbulence, *Phys. Rev. E* **95**, 033119 (2017).
- [50] S. Čopar, J. Aplinc, Z. Kos, S. Zumer, and M. Ravnik, Topology of Three-Dimensional Active Nematic Turbulence Confined to Droplets, *Phys. Rev. X* **9**, 031051 (2019).
- [51] G. De Magistris, A. Tiribocchi, C. Whitfield, R. Hawkins, M. Cates, and D. Marenduzzo, Spontaneous motility of passive emulsion droplets in polar active gels, *Soft Matter* **10**, 7826 (2014).
- [52] C. A. Whitfield, D. Marenduzzo, R. Voituriez, and R. J. Hawkins, Active polar fluid flow in finite droplets, *Europhys. J. E* **37**, 8 (2014).
- [53] F. Fadda, G. Gonnella, A. Lamura, and A. Tiribocchi, Lattice Boltzmann study of chemically driven self-propelled droplets, *Europhys. J. E* **40**, 112 (2017).
- [54] R. Singh, E. Tjhung, and M. E. Cates, Self-propulsion of active droplets without liquid-crystalline order, *Phys. Rev. Res.* **2**, 032024(R) (2020).
- [55] G. Gompper, R. G. Winkler, T. Speck, A. Solon, C. Nardini, F. Peruani, H. Löwen, R. Golestanian, U. B. Kaupp, L. Alvarez *et al.*, The 2020 motile active matter road map, *J. Phys.: Condens. Matter* **32**, 193001 (2020).
- [56] F. Ziebert, S. Swaminathan, and I. S. Aranson, Model for self-polarization and motility of keratocyte fragments, *J. R. Soc. Interface* **9**, 1084 (2012).
- [57] K. Dubrovinski and K. Kruse, Cell Motility Resulting from Spontaneous Polymerization Waves, *Phys. Rev. Lett.* **107**, 258103 (2011).
- [58] V. Ruprecht, S. Wieser, A. Callan-Jones, M. Smutny, H. Morita, K. Sako, V. Barone, M. Ritsch-Martel, M. Sixt, R. Voituriez *et al.*, Cortical contractility triggers a stochastic switch to fast amoeboid cell motility, *Cell* **160**, 673 (2015).
- [59] R. J. Hawkins, M. Piel, G. Faure-Andre, A. M. Lennon-Dumenil, J. F. Joanny, J. Prost, and R. Voituriez, Pushing off the Walls: A Mechanism of Cell Motility in Confinement, *Phys. Rev. Lett.* **102**, 058103 (2009).
- [60] I. S. Aranson, *Physical Models of Cell Motility* (Springer, New York, 2016).
- [61] D. Shao, H. Levine, and W.-J. Rappel, Coupling actin flow, adhesion, and morphology in a computational cell motility model, *Proc. Natl. Acad. Sci.* **109**, 6851 (2012).
- [62] L. Stankevics, N. Ecker, E. Terriac, P. Maiuri, R. Schoppmeyer, P. Vargas, A.-M. Lennon-Dumenil, M. Piel, B. Qu, M. Hoth *et al.*, Deterministic actin waves as generators of cell polarization cues, *Proc. Natl. Acad. Sci.* **117**, 826 (2020).